Materials Today Bio 27 (2024) 101137

Contents lists available at ScienceDirect

Materials Today Bio

journal homepage: www.journals.elsevier.com/materials-today-bio

Nickel atom-clusters nanozyme for boosting ferroptosis tumor therapy

Hongji Liu [a,b,1], Biao Yu [b,1], Can Zhou [c], Zhiming Deng [a], Hui Wang [b,*], Xin Zhang [b,*], Kai Wang [a,*]

[a] State Key Laboratory of Chemo/Biosensing and Chemometrics, College of Chemistry and Chemical Engineering, Hunan University, Changsha, 410082, Hunan, PR China

[b] High Magnetic Field Laboratory, Hefei Institutes of Physical Science, Chinese Academy of Sciences, Hefei 230031, Anhui, PR China

[c] Reproductive and Genetic Hospital of CITIC-Xiangya and Clinical Research Center for Reproduction and Genetics in Hunan Province, Changsha, Hunan, PR China

ARTICLE INFO

Keywords:
Ni-based nanozyme
Single-atom-metal-clusters
Ferroptosis
Tumor therapy

ABSTRACT

The translation of Fe-based agents for ferroptosis tumor therapy is restricted by the unstable iron valence state, the harsh catalytic environment, and the complex tumor self-protection mechanism. Herein, we developed a stable nickel-based single-atom-metal-clusters (NSAMCs) biocatalyst for efficient tumor ferroptosis therapy. NSAMCs with a nanowire-like nanostructure and hydrophilic functional groups exhibit good water-solubility, colloidal stability, negligible systemic toxicity, and target specificity. In particular, NSAMCs possess excellent peroxidase-like and glutathione oxidase-like activities through the synergistic influence between metal clusters and single atoms. The dual-enzymatic performance enables NSAMCs to synergistically promote efficient ferroptosis of cancer cells through lipid peroxidization aggregation and glutathione peroxidase 4 inactivation. Importantly, NSAMCs highlight the boost of ferroptosis tumor therapy *via* the synergistic effect between single-atoms and metal clusters, providing a practical and feasible paradigm for further improving the efficiency of ferroptosis tumor treatment.

1. Introduction

Ferroptosis, divergent from autophagy, necrosis, and apoptosis, is a unique pathway of regulated cell death [1–4]. Lipid peroxidation (LPO) caused by iron-induced hydroxyl radicals (•OH) is the driving force of ferroptosis, leading to dysregulated levels of intracellular oxidation and subsequent cell death [5–9]. Notably, ferroptosis has excellent translational prospects in anti-tumor therapy since this unique cell death pathway bypasses the resistance of conventional therapies [10–12]. To date, numerous iron-based nanoadjuvants have been explored as tumor ferroptosis drugs [13–18]. For example, hierarchically iron architecture shows switchable magnetic resonance imaging and effective ferroptosis, providing a paradigm for companion diagnostics [19]. A FeS_2 nanozyme modified by polyvinyl pyrrolidone shows dual-enzymatic activity, provoking available apoptosis and ferroptosis [20]. However, the intracellular unstable divalent iron pools and stringent catalytic conditions weaken the tumor therapeutic efficiency of iron-based nanoagents [21,22]. Therefore, developing stable non-iron-based nanotherapeutics is crucial for ferroptosis tumor therapy.

Recently, the transition metal nickel (Ni)-based catalysts have attracted much attention due to their relatively stable valence state and the ability to catalyze the formation of •OH [23,24]. However, the compromised catalytic performance induced by the high free energy hinders the biomedical applications of Ni-based catalysts [25]. Specifically, single-atom-catalysts (SACs) have solved the aforementioned difficulty since the tall dispersion of metal sites and have manifested promising potential in antitumor fields [26–28]. Nevertheless, the therapeutic effect of SAC nanomedicines is unsatisfactory due to the number limitation of active sites [29]. Very recently, researchers have reported that the synergistic effect between SACs and supporting metal clusters is conducive to further improving the catalytic performance of SACs [30,31]. For example, Xu et al. reported that the interaction of SACs with supporting metal clusters resulted in charge accumulation, stronger adsorption, and better catalytic activity [32]. Therefore, it is meaningful to fabricate a stable, efficient Ni-based single--atom-metal-clusters (SAMCs) nanomedicine for further inhibiting the proliferation of malignant tumors.

Here, we reported a kind of g-C_3N_4 (CN) supported Ni SAMCs

* Corresponding authors.
E-mail addresses: hw39@hmfl.ac.cn (H. Wang), xinzhang@hmfl.ac.cn (X. Zhang), hyxj0309@163.com (K. Wang).
[1] These authors contributed equally to this work.

https://doi.org/10.1016/j.mtbio.2024.101137
Received 6 April 2024; Received in revised form 12 June 2024; Accepted 22 June 2024
Available online 22 June 2024

(NSAMCs) with excellent aqueous dispersibility and long-term stability, which was prepared by pyrolysis of formamide followed by *in situ* reduction of nickel chloride. NSAMCs with both peroxidase (POD)-like behavior and glutathione oxidase (GSHOD)-like performance, can realize efficiently ferroptosis-mediated tumor therapy. The excellent dual-enzymatic activities originate from the synergistic effect between Ni atoms and Ni clusters. The synergistic cooperation between LPO accumulation caused by NSAMC-mediated •OH generation and glutathione peroxidase 4 (GPx-4) inactivation triggered by NSAMC's GSHOD-like activity leads to boost tumor ferroptosis. The investigations have shown that NSAMCs have negligible systemic toxicity, excellent target specificity, and a high tumor suppression rate. Importantly, NSAMCs provide a possibility to further promote the clinical practice of tumor ferroptosis therapy.

2. Experimental methods

2.1. Preparation of NSAMCs

30 mL of formamide solution containing $NiCl_2{\cdot}6H_2O$ (0.713 g) was stirred for 20 min at 500 rpm at 25 °C. Next, the mixture was changed into a 50 mL autoclave (Anhui Kemi Instrument Co., Ltd). The sealed vessel was warmed at 200 °C for one whole day. After cooling down to 25 °C, the supernatant was gathered by centrifugation and dialyzed (100,000 Da) for 3 days to remove the unreacted precursors. The aqueous dispersion of NSAMCs was spun down for 10 min at 12,000 rpm, cleaned with ethanol and water for 3 times successively, and then dried at 50 °C for 6 h.

Details about enzymatic reaction tests, catalyst characterizations, and *in vivo* and *in vitro* experiments, are presented in the Supporting Information.

3. Results and discussion

3.1. Construction and characterization of NSAMCs

The NSAMCs were prepared *via* a one-pot solvothermal process, where the dispersion of $NiCl_2{\cdot}6H_2O$ in formamide was treated at 200 °C for 24 h. The nanowire profile of NSAMCs was determined *via* transmission electron microscopy (TEM), and the results showed that the length of NSAMCs was approximately 250 nm and the width was approximately 40 nm (Fig. 1a and Fig. S1). Also, the hydrodynamic size of NSAMCs measured *via* dynamic light scattering was consistent with the TEM test results (Fig. S2). The large-scale high-angle annular dark field (HAADF) suggested the existence of Ni nanoparticles was not found (Fig. 1b). Additionally, the relevant elemental representation exhibited that Ni species were uniformly distributed on the CN matrix (Fig. 1c). Furthermore, the isolation performance of Ni species was discerned by the aberration-corrected high-angle annular dark-field scanning transmission electron microscopy (AC-HAADF-STEM). As shown in Fig. 1d, Ni atoms (highlighted by yellow dashed circles), as well as Ni clusters (prominented by green circles) were evenly distributed on the CN substrate. Moreover, the Ni signals were surrounded by N species (Fig. 1e and f, and Fig. S3) according to the EELS mapping results with a nanoscale resolution, indicating that Ni atoms or clusters could coordinate with N atoms. X-ray diffraction pattern showed a sharp peak at 26.7° (Fig. S4), which should come from amorphous CN [33,34]. In addition, No other obvious peak was observed, indicating again the absence of lager-size Ni nanoparticles in NSAMCs [35]. The above program indicates that the Ni species in NSAMCs contains both single atoms and atom clusters.

The Ni content in NSAMCs was 6.48 wt% *via* inductively coupled plasma atomic emission spectrometry (ICP-AES). The disordered domains (1362 cm^{-1}) in the Raman spectrum (Fig. S5) and the N vacancy in electron paramagnetic resonance (EPR, Fig. S6) indicated that there existed vacancy structures to stabilize Ni species [36,37]. The

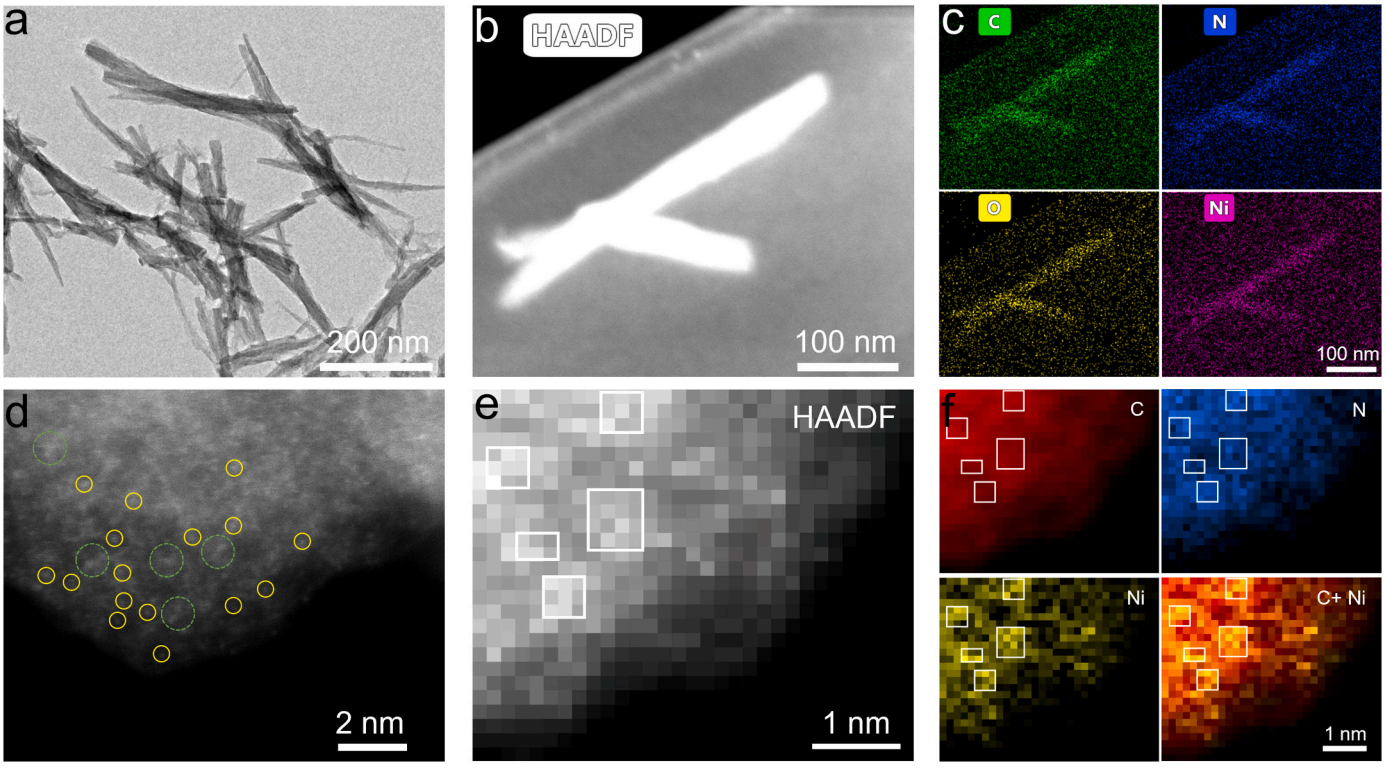

Fig. 1. Morphology and structure of NSAMCs. a, TEM image of NSAMCs. b and c, HAADF-STEM image and corresponding EDX mapping images of NSAMCs. d, AC-HAADF-STEM image of NSAMCs. e and f, EDX elemental mapping of C, N, and Ni in NSAMCs.

coordination environment of Ni species was detected *via* X-ray absorption fine structure (XAFS) and X-ray absorption near-edge structure (XANES). As shown in Fig. 2a, the Ni–N_4 moieties existed in NSAMCs due to the similar pre-edge peak between NSAMCs and NiPc. In addition, the coordination environment of NSAMCs was determined *via* Fourier transform (FT) extended-XAFS (EXAFS). The minor peak of NSAMCs (1.47 Å) attributed to Ni–N first shell coordination and the main peak at 2.52 Å satisfactorily interpreted as Ni–Ni contribution was observed in EXAFS (Fig. 2b), indicating that the Ni species contains both single atoms and clusters. The Fourier-transform infrared (FT-IR) spectrum demonstrated that there were multiple fingerprint peaks of heptazine rings (1100 - 1600 cm^{-1}) and tri-*s*-triazine rings (802 cm^{-1}) in CN (Fig. 2c) [38,39]. Simultaneously, a prominent absorption peak at 3344 cm^{-1} from hydrophilic groups was observed, endowing NSAMCs with excellent water solubility and long-term stability in 1*PBS and cell culture medium (Fig. S7) [40]. The X-ray photoelectron spectroscopy (XPS) survey in Fig. S8 indicated that C, N, O, and Ni elements existed on the surface of NSAMCs, and the atomic ratio of Ni was 1.35 %. The C 1s spectrum (Fig. 2d) of NSAMCs could be deconvoluted into three peaks, i.e., C–C (sp^3), C–N or C–O (sp^3), and C═O (sp^2) [41,42]. The N 1s fingerprint spectrum could be fitted to graphene N, pyridine N, and pyrrolic N, respectively (Fig. 2e) [43,44]. The Ni 2p spectrum could be designated as Ni $2p_{3/2}$ and Ni $2p_{1/2}$, with two corresponding satellite peaks, characteristic of Ni^{2+} (Fig. 2f) [45,46]. The O1s XPS spectrum (Fig. S9) could be fitted into C═O, C–O, and C–O–C peaks, respectively [47,48].

3.2. Enzyme-like performance of NSAMCs

Ni ions can be applied to initiate the Fenton-like reaction. The downstream product of the POD-like performance of NSAMCs was determined by EPR technology using 5,5-dimethyl-1-pyrroline N-oxide (DMPO) as a spin-trap molecule. The typical DMPO-•OH characteristic peak curve indicated that NSAMCs could specifically recognize tumor microenvironment (TME) and generate highly toxic •OH (Fig. 3a). Furthermore, the intensity of the generated •OH signal became more pronounced as the NSAMCs dose increases (Fig. S10). Consequently, we detected the enzymatic kinetics of NSAMC-catalyzed •OH using 3,3′,5,5′-tetramethylbenzidine (TMB) as an optical sensor. The reaction of TMB with the product of the POD-like activity of NSAMCs could produce an evident color change (Figs. S11 and S12), and the formed oxidized-TMB signal intensity increased over time (Fig. S13).

We then evaluated the rate of •OH generation *via* the Michaelis-Menten constant (K_M) and the maximum initial velocity (V_{max}). As illustrated in Fig. 3b and S14, when the H_2O_2 was used as the substrate, the fitted values of the V_{max} and K_M were 0.117 μM/s and 72.35 mM, respectively. When the reaction substrate was changed to TMB, the values of V_{max} and K_M fitted values were 0.052 μM/s and 0.169 mM, respectively (Fig. S15). In addition, the specific activity (SA) value of NSAMCs was calculated to be 35.46 U mg^{-1} (Fig. S16). Both pH and temperature, as two major factors affecting POD mimetics, also affect the enzymatic performance of NSAMCs. The results indicated optimal conditions for the POD-like activity of NSAMCs were pH 3.5 and 50 °C (Fig. 3c and S17). The overexpression of GSH within TME makes tumor cells resistant to catalytic therapy [49]. Fortunately, high valence metals can consume GSH, thereby enhancing the progression of tumor ferroptosis [50]. We evaluated the depletion potential of NSAMCs on GSH *via* the ^1H NMR and GSH kit. As shown in Fig. 3d, it could be observed that the integral strength of disulfide bonds in ^1H NMR gradually becomes apparent over time after the feeding of NSAMCs, indicating that NSAMCs could effectively consume GSH. The colorimetric experiments with parameters of time and concentration showed that NSAMCs could serve as an excellent GSHOD-like reagent (Fig. 3e and S18). Furthermore, the SA value of GSHOD-like activity of NSAMCs was determined by fitting to be 1.73 U mg^{-1} (Fig. S19), which is higher than the reported Fe-based nanozymes [51]. In addition, thermogravimetric analysis illustrated that NSAMCs had excellent thermal stability (Fig. S20). The above procedure indicates that NSAMCs possesses excellent POD- and

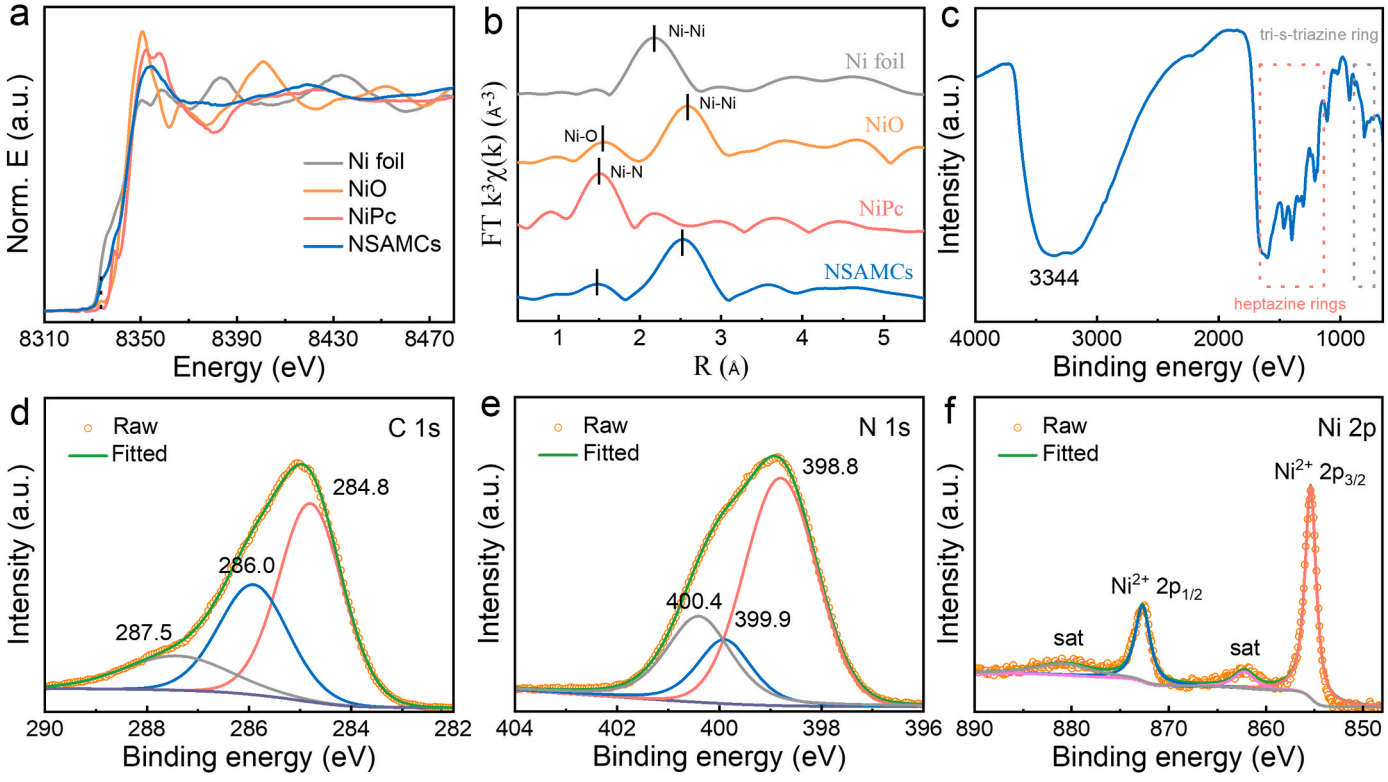

Fig. 2. Phase and surface properties of NSAMCs. a, XANES spectra of NSAMCs. b, FT EXAFS spectra of NSAMCs. c, FT-IR spectrum of NSAMCs. d-f, XPS spectra of C 1s (d), N1s (e), and Ni 2p (f).

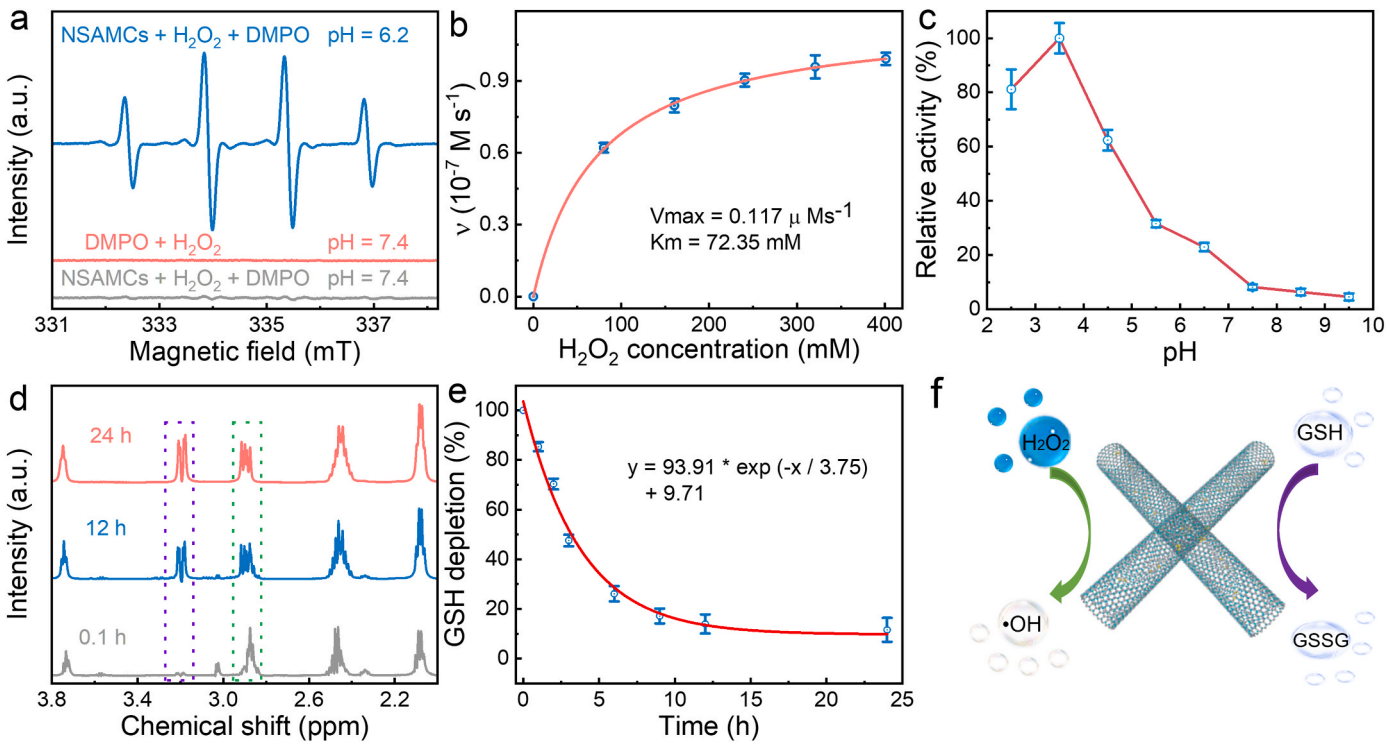

Fig. 3. Catalytic properties of NSAMCs. a, EPR spectra of •OH in various reaction systems using DMPO as a trapping agent. b, Kinetics for POD-like activity of NSAMCs against H_2O_2 concentrations. c, POD-like performance of NSAMCs against pH value. d, ^1H NMR spectra of GSH reacted with NSAMCs. e, GSH depletion performance of NSAMCs at various times. f, Schematic illustration of the POD-like and GSHOD-like function of NSAMCs.

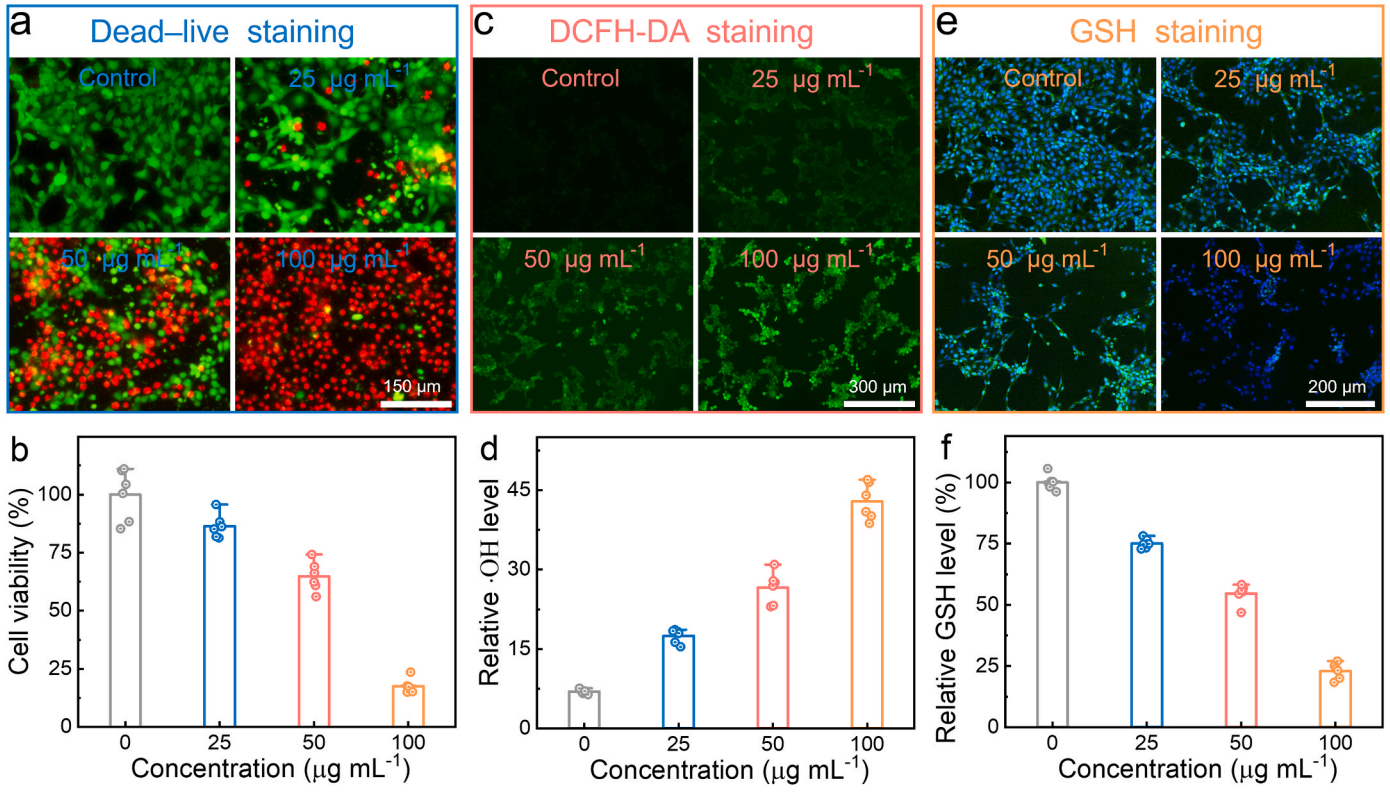

Fig. 4. *In vitro* therapy of NSAMCs. a, Fluorescence images of dead-living staining at different densities of NSAMCs; (b) 4T1 cell viability against NSAMCs at pH 6.2 (n = 6). (c) Fluorescence images of DCFH-DA staining at different densities of NSAMCs; (d) Quantitative analysis of intracellular •OH level. Labeling indexes were read from 6 random fields *via* ImageJ software. (e) Fluorescence images of GSH kit staining at different densities of NSAMCs; (f) Quantitative analysis of intracellular GSH level. Labeling indexes were read from 6 random fields *via* ImageJ software.

GSHOD-like catalytic properties, showing great prospects in ferroptosis tumor treatment (Fig. 3f).

3.3. In vitro antitumor performance of NSAMCs

Based on the efficient •OH generation ability and GSH depletion performance, we further tested the inhibitory effect of NSAMCs on cancer cells *in vitro*. The confocal imaging of live-dead staining showed that the red signal representing dead cells became increasingly evident in a concentration-dependent manner (Fig. 4a). The survival rate of cancer cells was 17.58 %, while the incubation dose of NSAMCs reached 100 μg mL^{-1} (Fig. 4b), detected *via* Cell Titer-Glo luminescent kit assay. The significant inhibitory effect is most likely due to the *in situ* production of •OH by NSAMCs in tumor cells, as well as the downregulation of GSH. As expected, a green fluorescence signal became gradually obvious as the incubation concentration of NSAMCs increased (Fig. 4c and d), indicating that NSAMCs catalyze H_2O_2 in cancer cells to produce highly toxic •OH. Moreover, the intracellular attenuation of GSH expression resulted in an unbalanced oxidative steady state in tumor cells (Fig. 4e and f). The GSH/GSSG content in cancer cells treated with NSAMCs was further quantified by GSH kit and showed that the ratio was related to the concentration of nanoadjuvant, reconfirming the great potential of NSAMCs as GSHOD-like enzyme (Fig. S21).

The cell death pathway showed that the GPx-4 in tumor cells decreased, illustrating the superior GSHOD-like capability of NSAMCs (Fig. 5a). In addition, the induction of apoptosis also contributed to the growth inhibition of 4T1 cells, which was collectively manifested by the cleaved caspase-3 and cleaved PARP levels after treatment with NSAMCs (Fig. 5b). The accumulation of highly toxic •OH leaded to significant increase of LPO level in cancer cells while the GSHOD-like activity of NSAMCs mediated the GPx-4 inactivation (Fig. 5c and d), leading to ferroptosis of 4T1 cells. We further evaluated the two products of LPO, namely 4-hydroxynonenal (4-HNE) and malondialdehyde (MDA), respectively. Both indicators showed significant upregulation levels in a concentration-dependent manner (Fig. 5e and f), indicating the NSAMCs induced 4T1 cell death *via* ferroptosis. Collectively, NSAMCs exert POD-like and GSHOD-like activities, leading to •OH burst and GSH consumption, disrupting the homeostasis of cancer cells, mediating LPO accumulation and GPx-4 inactivation, and ultimately leading to cell death.

3.4. Biosafety analysis of NSAMCs

The biosafety of NSAMCs was investigated in cellular and mouse models. The cell viability remained above 90 % after incubating with NSAMCs in a neutral medium for 72 h (Fig. S22). The accumulation and metabolism of NSAMCs in major organs were obtained by *ex vivo* tissue disruption treatment of mice (Fig. S23). The NSAMCs primarily accumulated in the liver and heart, and gradually weakened over time, demonstrating an efficient excretion of NSAMCs. Notably, the Ni intensity in tumor site became more accumulative at 48 h post-injection based on the enhanced permeability and retention effect [52]. The blood half-life was calculated to be 2.19 h *via* ExpDec2 curve fitting (Fig. S24 a), verifying again that NSAMCs could be rapidly cleared by *in vivo* circulatory system. The elimination rate curve constants of the two stages were −0.32 and −0.011 μg mL^{-1} h^{-1}, respectively, revealing the rapid scavenging property of NSAMCs (Fig. S24 b). No meaningful difference in the blood markers, including alkaline phosphatase (ALP), alanine aminotransferase (ALT), Urea, Crea, white blood cells, and red blood cells, was detected between the NSAMC-treated mice and the control group (Figs. S25–27). Furthermore, tissue section analysis showed that the major organs of mice from the NSAMC-treated group were morphologically normal, without significant damage (Fig. S28). Collectively, these findings indicate that the risk of NSAMC exudation was negligible.

3.5. The antitumor efficacy in vivo of NSAMCs

Subsequently, the tumor suppressive effect of NSAMCs was demonstrated in the 4T1-xenograft tumor mice model (Fig. 6a). Six-week-old mice model were randomized into 3 groups when their tumors reached about 60 mm^3, and received an equal volume of tail vein

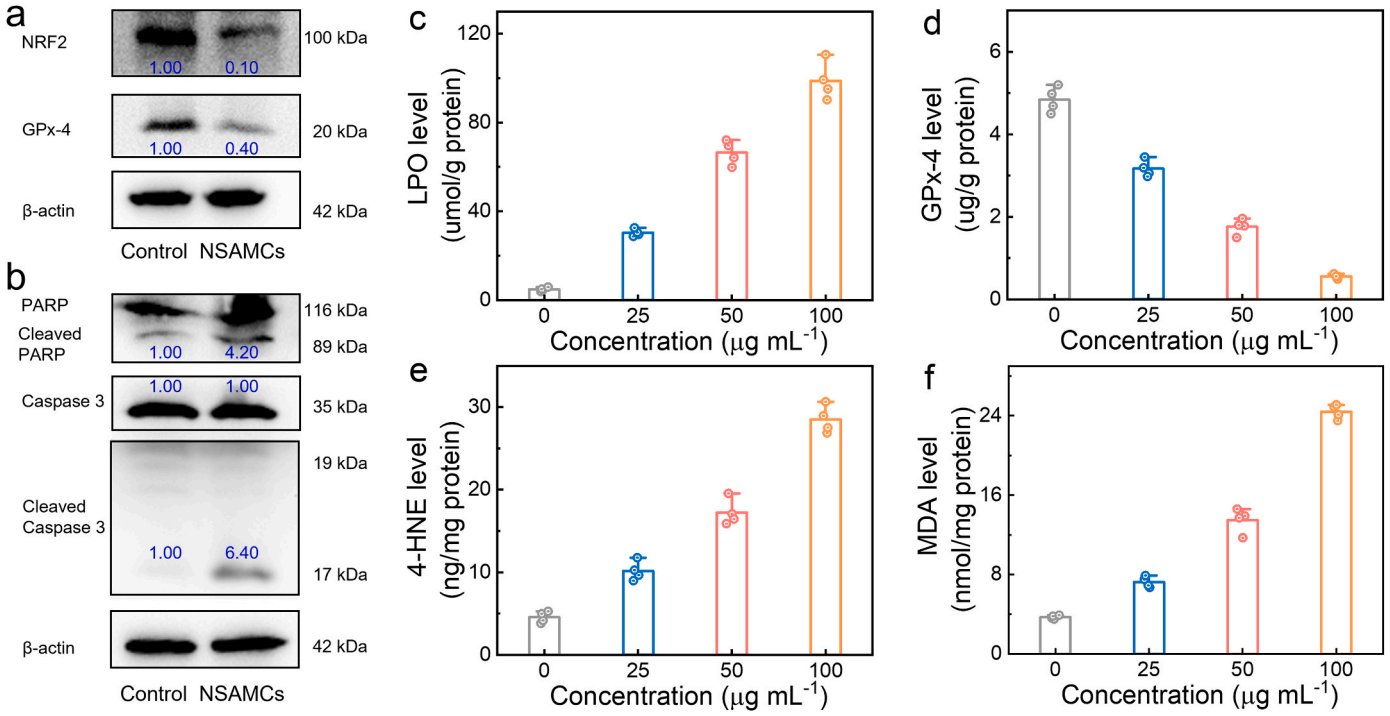

Fig. 5. NSAMCs induced 4T1 cells ferroptosis. a, b Western blotting assay of the representative protein expression after different treatments with PBS or NSAMCs (50 μg mL^{-1}). c-f, LPO level (c), GPx-4 level (d), 4-HNE level (e), and MDA activity (f) measured after treatment with various doses of NSAMCs (n = 4).

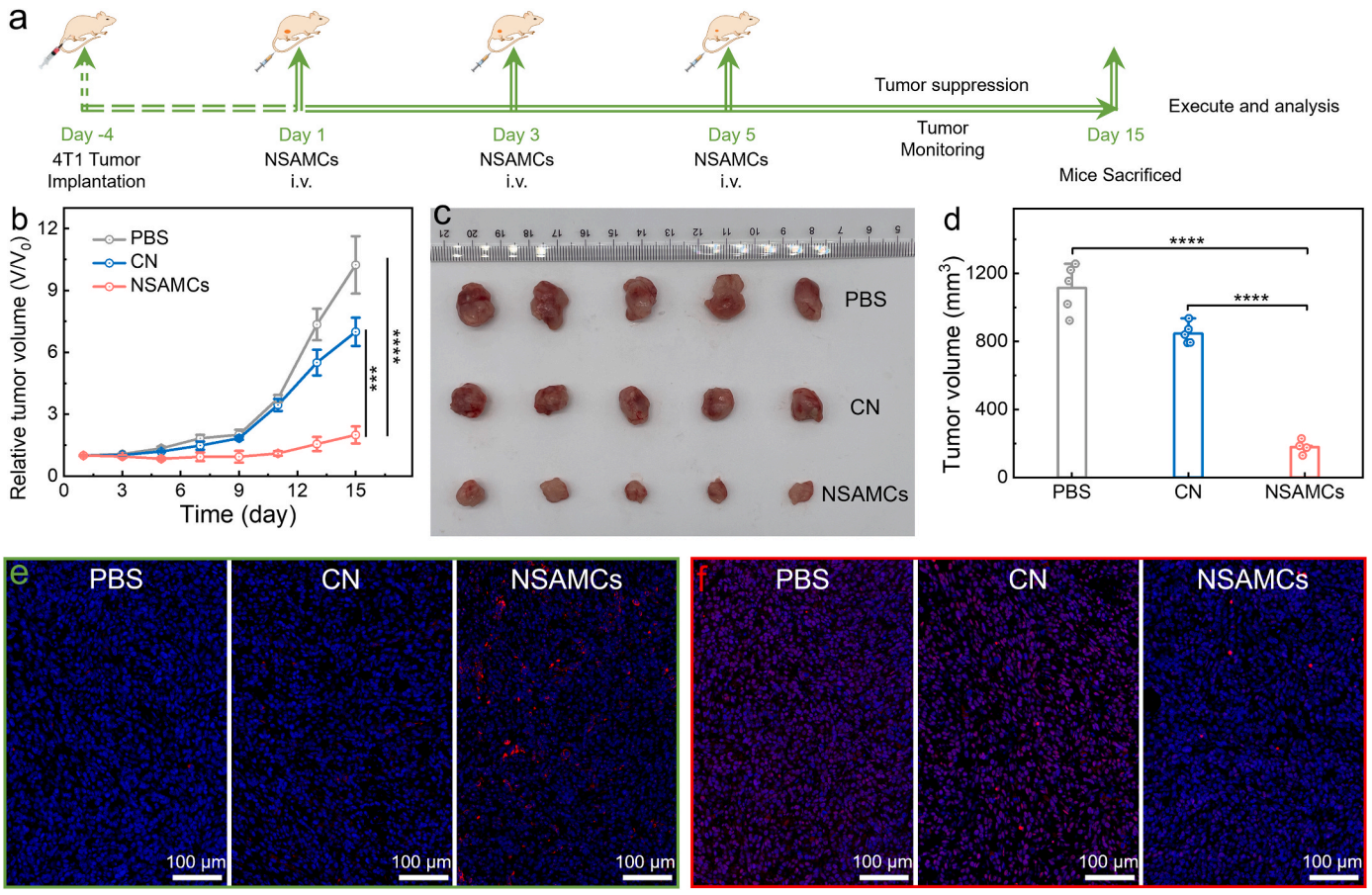

Fig. 6. *In vivo* therapy of NSAMCs. a, The treatment procedure of NSAMCs. b, Relative tumor volume curves of 4T1-tumor-bearing mice. c, Photo of extracted tumors. d, Average volume of the tumors harvested from mice receiving various handles. e, f Immunofluorescence staining: LPO staining (e), GPx-4 staining (f).

injections of I: PBS, II: CN, and III: NSAMCs. As shown in Fig. 6b and c, mice from PBS- or CN-treated groups exhibited rapid tumor growth. In contrast, the tumor growth in NSAMC-treated mice was effectively inhibited with a tumor inhibition rate of 84.32 % (Fig. S29), intimating the specific tumor-catalytic therapy effect of NSAMCs. Moreover, both tumor mass and volume statistics revealed that NSAMC could effectively inhibit tumor proliferation (Fig. 6d and S30). Furthermore, the body weight showed no significant abnormality during the treatment, further indicating the negligible toxicity of NSAMCs (Fig. S31).

Histopathological analysis of the mice tumors showed that only the NSAMC-treated group displayed apparent structural damage, while the PBS- and CN-treated groups had normal morphology (Fig. S32). When the tumor was treated for seven days, the tumor was harvested, and LPO and GPx-4 levels were examined. As shown in Fig. 6e and f, tumor sections of mice from different treatment groups showed that NSAMCs could effectively lead to the accumulation of LPO and inactivation of GPx-4, suggesting the occurrence of ferroptosis in 4T1 tumors. In addition, the up-regulation of LPO-positive signals and destabilization of GPx-4 indicated higher levels of cell ferroptosis (Figs. S33 and S34). The above findings indicate that NSAMCs with POD-like and GSHOD-like performance can efficiently inhibit tumor proliferation by synergistically mediating LPO aggregation and GPx-4 downregulation.

4. Conclusion

In summary, we have successfully developed a stable, efficient, and biologically benign Ni-based biocatalyst (NSAMCs) for enhanced tumor ferroptosis therapy. Such NSAMCs exhibit enhanced POD-like activity and GSHOD-like enzymatic performance, attributed to the mutual promotion between single atoms and metal clusters. In TME, NSAMCs efficiently break the O–O bond in H_2O_2 to produce •OH, and can oxidize GSH to GSSG, thus promoting synergistically induced ferroptosis in tumor cells. Experiments showed that NSAMCs with negligible off-target toxicity could efficiently inhibit tumor proliferation with an inhibition rate of 84.32 %. The mechanism of tumor cell death had been verified as LPO accumulation and GPx-4 inactivation caused by efficient production of •OH and down-regulation of GSH, further leading to ferroptosis. The NSAMCs will provide a practical and feasible strategy to boost ferroptosis tumor therapy.

CRediT authorship contribution statement

Hongji Liu: Writing – review & editing, Writing – original draft, Visualization, Validation, Investigation, Funding acquisition, Formal analysis, Conceptualization. **Biao Yu:** Visualization, Validation. **Can Zhou:** Visualization, Validation, Investigation, Formal analysis. **Zhiming Deng:** Supervision. **Hui Wang:** Writing – review & editing, Writing – original draft, Visualization, Supervision, Resources, Project administration, Methodology, Funding acquisition, Formal analysis, Conceptualization. **Xin Zhang:** Supervision, Resources, Project administration, Funding acquisition. **Kai Wang:** Supervision, Resources, Project administration.

Declaration of competing interest

The authors declare the following financial interests/personal relationships which may be considered as potential competing interests: Hui Wang reports financial support was provided by Ministry of Science and Technology of the People's Republic of China. Hongji Liu reports financial support was provided by China Postdoctoral Science

Foundation. Xin Zhang reports financial support was provided by National Natural Science Foundation of China. Hui Wang reports financial support was provided by Anhui Provincial Natural Science Foundation. If there are other authors, they declare that they have no known competing financial interests or personal relationships that could have appeared to influence the work reported in this paper.

Data availability

Data will be made available on request.

Acknowledgments

This work was funded by financial support from the National Key R&D Program of China (Grant No. 2021YFA1600202), the fellowship of China National Postdoctoral Program for Innovative Talents (BX20230111), National Natural Science Foundation of China (U21A20148), Anhui Provincial Natural Science Foundation (2308085J18).

Appendix A. Supplementary data

Supplementary data to this article can be found online at https://doi.org/10.1016/j.mtbio.2024.101137.

References

[1] B.R. Stockwell, Ferroptosis turns 10: emerging mechanisms, physiological functions, and therapeutic applications, Cell 185 (2022) 2401–2421.
[2] U. Harjes, Therapeutic resistance: ironing it out, Nat. Rev. Cancer 17 (2017) 510.
[3] K. Hadian, B.R. Stockwell, A roadmap to creating ferroptosis-based medicines, Nat. Chem. Biol. 17 (2021) 1113–1116.
[4] Q. Fan, W. Xiong, H. Zhou, J. Yang, J. Feng, Z. Li, L. Wu, F. Hu, X. Duan, B. Li, J. Fan, Y. Xu, X. Chen, Z. Shen, An and logic gate for magnetic-resonance-imaging-guided ferroptosis therapy of tumors, Adv. Mater. 35 (2023) e2305932.
[5] H. Liu, Z. Deng, Z. Zhang, W. Lin, M. Zhang, H. Wang, Graphene quantum dots as metal-free nanozymes for chemodynamic therapy of cancer, Matter 7 (2024) 977–990.
[6] C. Wu, Z. Liu, Z. Chen, D. Xu, L. Chen, H. Lin, J. Shi, A nonferrous ferroptosis-like strategy for antioxidant inhibition–synergized nanocatalytic tumor therapeutics, Sci. Adv. 7 (2021) eabj8833.
[7] J. Yang, R. Zhang, H. Zhao, H. Qi, J. Li, J. Li, X. Zhou, A. Wang, K. Fan, X. Yan, T. Zhang, Bioinspired copper single-atom nanozyme as a superoxide dismutase-like antioxidant for sepsis treatment, Exploration 2 (2022) 20210267.
[8] L. Huang, J. Zhu, W. Xiong, J. Feng, J. Yang, X. Lu, Y. Lu, Q. Zhang, P. Yi, Y. Feng, S. Guo, X. Qiu, Y. Xu, Z. Shen, Tumor-generated reactive oxygen species storm for high-performance ferroptosis therapy, ACS Nano 17 (2023) 11492–11506.
[9] S. Guo, W. Xiong, J. Zhu, J. Feng, R. Zhou, Q. Fan, Q. Zhang, Z. Li, J. Yang, H. Zhou, P. Yi, Y. Feng, S. Yang, X. Qiu, Y. Xu, Z. Shen, A STING pathway-activatable contrast agent for MRI-guided tumor immunoferroptosis synergistic therapy, Biomaterials 302 (2023) 122300.
[10] S. Liu, M. Zhang, H. Jin, Z. Wang, Y. Liu, S. Zhang, H. Zhang, Iron-containing protein-mimic supramolecular iron delivery systems for ferroptosis tumor therapy, J. Am. Chem. Soc. 145 (2023) 160–170.
[11] H. Liang, X. Wu, G. Zhao, K. Feng, K. Ni, X. Sun, Renal clearable ultrasmall single-crystal Fe nanoparticles for highly selective and effective ferroptosis therapy and immunotherapy, J. Am. Chem. Soc. 143 (2021) 15812–15823.
[12] T. Liu, W. Liu, M. Zhang, W. Yu, F. Gao, C. Li, S.B. Wang, J. Feng, X.Z. Zhang, Ferrous-supply-regeneration nanoengineering for cancer-cell-specific ferroptosis in combination with imaging-guided photodynamic therapy, ACS Nano 12 (2018) 12181–12192.
[13] C. Liang, X. Zhang, M. Yang, X. Dong, Recent progress in ferroptosis inducers for cancer therapy, Adv. Mater. 31 (2019) e1904197.
[14] F. Zeng, S. Nijiati, L. Tang, J. Ye, Z. Zhou, X. Chen, Ferroptosis detection: from approaches to applications, Angew. Chem. Int. Ed. 62 (2023) e202300379.
[15] H. Pan, S. Yang, Y.-E. Wang, Q.T.H. Shubhra, Ferroptosis-based image-guided chemotherapy, Matter 6 (2023) 666–668.
[16] L. Huang, J. Feng, J. Zhu, J. Yang, W. Xiong, X. Lu, S. Chen, S. Yang, Y. Li, Y. Xu, Z. Shen, A strategy of Fenton reaction cycloacceleration for high-performance ferroptosis therapy initiated by tumor microenvironment remodeling, Adv. Healthc. Mater. 12 (2023) e2203362.
[17] H. Peng, F. Yao, J. Zhao, W. Zhang, L. Chen, X. Wang, P. Yang, J. Tang, Y. Chi, Unraveling mitochondria-targeting reactive oxygen species modulation and their implementations in cancer therapy by nanomaterials, Exploration 3 (2023) 20220115.
[18] C. Wu, D. Xu, M. Ge, J. Luo, L. Chen, Z. Chen, Y. You, Y.-x. Zhu, H. Lin, J. Shi, Blocking glutathione regeneration: inorganic NADPH oxidase nanozyme catalyst potentiates tumoral ferroptosis, Nano Today 46 (2022) 101574.
[19] B. Yang, Y. Zhang, L. Sun, J. Wang, Z. Zhao, Z. Huang, W. Mao, R. Xue, R. Chen, J. Luo, T. Wang, J. Jiang, Y. Qin, Modulated ultrasmall γ-Fe_2O_3 nanocrystal assemblies for switchable magnetic resonance imaging and photothermal-ferroptotic-chemical synergistic cancer therapy, Adv. Funct. Mater. 33 (2022) 2211251.
[20] X. Meng, D. Li, L. Chen, H. He, Q. Wang, C. Hong, J. He, X. Gao, Y. Yang, B. Jiang, G. Nie, X. Yan, L. Gao, K. Fan, High-performance self-cascade pyrite nanozymes for apoptosis-ferroptosis synergistic tumor therapy, ACS Nano 15 (2021) 5735–5751.
[21] T. Zuo, T. Fang, J. Zhang, J. Yang, R. Xu, Z. Wang, H. Deng, Q. Shen, pH-sensitive molecular-switch-containing polymer nanoparticle for breast cancer therapy with ferritinophagy-cascade ferroptosis and tumor immune activation, Adv. Healthc. Mater. 10 (2021) e2100683.
[22] X. Zhang, X. Chen, Y. Zhao, Nanozymes: versatile platforms for cancer diagnosis and therapy, Nano-Micro Lett. 14 (2022) 95.
[23] Y. Qian, J. Zhang, J. Zou, X. Wang, X. Meng, H. Liu, Y. Lin, Q. Chen, L. Sun, W. Lin, H. Wang, NIR-II responsive pegylated nickel nanoclusters for photothermal enhanced chemodynamic synergistic oncotherapy, Theranostics 12 (2022) 3690–3702.
[24] Y. Zhu, W. Wang, P. Gong, Y. Zhao, Y. Pan, J. Zou, R. Ao, J. Wang, H. Cai, H. Huang, M. Yu, H. Wang, L. Lin, X. Chen, Y. Wu, Enhancing catalytic activity of a nickel single atom enzyme by polynary heteroatom doping for ferroptosis-based tumor therapy, ACS Nano 17 (2023) 3064–3076.
[25] F. Wang, B. Han, L. Zhang, L. Xu, H. Yu, W. Shi, CO_2 reforming with methane over small-sized Ni@SiO_2 catalysts with unique features of sintering-free and low carbon, Appl. Catal. B Environ. 235 (2018) 26–35.
[26] M. Huo, L. Wang, Y. Wang, Y. Chen, J. Shi, Nanocatalytic tumor therapy by single-atom catalysts, ACS Nano 13 (2019) 2643–2653.
[27] M. Chang, Z. Hou, M. Wang, C. Yang, R. Wang, F. Li, D. Liu, T. Peng, C. Li, J. Lin, Single-atom Pd nanozyme for ferroptosis-boosted mild-temperature photothermal therapy, Angew. Chem. Int. Ed. 60 (2021) 12971–12979.
[28] Y. Zhu, W. Wang, J. Cheng, Y. Qu, Y. Dai, M. Liu, J. Yu, C. Wang, H. Wang, S. Wang, C. Zhao, Y. Wu, Y. Liu, Stimuli-responsive manganese single-atom nanozyme for tumor therapy via integrated cascade reactions, Angew. Chem. Int. Ed. 60 (2021) 9480–9488.
[29] H. Liu, B. Yu, J. Shi, X. Peng, W. Zhou, K. Wang, X. Zhang, H. Wang, Ultrahigh density copper (I) single atom enzymes for tumor self-cascade catalytic therapy, Chem. Eng. J. 480 (2024) 148273.
[30] H. Liu, X. Lang, C. Zhu, J. Timoshenko, M. Ruscher, L. Bai, N. Guijarro, H. Yin, Y. Peng, J. Li, Z. Liu, W. Wang, B.R. Cuenya, J. Luo, Efficient electrochemical nitrate reduction to ammonia with copper-supported rhodium cluster and single-atom catalysts, Angew. Chem. Int. Ed. 61 (2022) e202202556.
[31] M. Liu, J. Lee, T.C. Yang, F. Zheng, J. Zhao, C.M. Yang, L.Y.S. Lee, Synergies of fe single atoms and clusters on N-doped carbon electrocatalyst for pH-universal oxygen reduction, Small Methods 5 (2021) e2001165.
[32] M. Zhang, H. Li, J. Chen, F.X. Ma, L. Zhen, Z. Wen, C.Y. Xu, High-loading Co single atoms and clusters active sites toward enhanced electrocatalysis of oxygen reduction reaction for high-performance Zn-Air battery, Adv. Funct. Mater. 33 (2022) 2209726.
[33] Y. Xiong, W. Sun, P. Xin, W. Chen, X. Zheng, W. Yan, L. Zheng, J. Dong, J. Zhang, D. Wang, Y. Li, Gram-scale synthesis of high-loading single-atomic-site Fe catalysts for effective epoxidation of styrene, Adv. Mater. 32 (2020) 2000896.
[34] G. Wang, R. Huang, J. Zhang, J. Mao, D. Wang, Y. Li, Synergistic modulation of the separation of photo-generated carriers via engineering of dual atomic sites for promoting photocatalytic performance, Adv. Mater. 33 (2021) 2105904.
[35] C. Pan, F. Wu, J. Mao, W. Wu, G. Zhao, W. Ji, W. Ma, P. Yu, L. Mao, Highly stable and selective sensing of hydrogen sulfide in living mouse brain with NiN_4 single-atom catalyst-based galvanic redox potentiometry, J. Am. Chem. Soc. 144 (2022) 14678–14686.
[36] Y. Zuo, T. Li, N. Zhang, T. Jing, D. Rao, P. Schmuki, S. Kment, R. Zboril, Y. Chai, Spatially confined formation of single atoms in highly porous carbon nitride nanoreactors, ACS Nano 15 (2021) 7790–7798.
[37] S. Wang, Z. Qian, Q. Huang, Y. Tan, F. Lv, L. Zeng, C. Shang, K. Wang, G. Wang, Y. Mao, Y. Wang, Q. Zhang, L. Gu, S. Guo, Industrial-level CO_2 electroreduction using solid-electrolyte devices enabled by high-loading nickel atomic site catalysts, Adv. Energy Mater. 12 (2022) 2201278.
[38] W. Xie, K. Li, X.H. Liu, X. Zhang, H. Huang, P-mediated Cu-N_4 sites in carbon nitride realizing CO_2 photoreduction to C_2H_4 with selectivity modulation, Adv. Mater. 35 (2023) e2208132.
[39] G. Wang, Z. Chen, T. Wang, D. Wang, J. Mao, P and Cu dual sites on graphitic carbon nitride for photocatalytic CO_2 reduction to hydrocarbon fuels with high C_2H_6 evolution, Angew. Chem. Int. Ed. 61 (2022) e202210789.
[40] H. Liu, X. Lv, J. Qian, H. Li, Y. Qian, X. Wang, X. Meng, W. Lin, H. Wang, Graphitic carbon nitride quantum dots embedded in carbon nanosheets for near-infrared imaging-guided combined photo-chemotherapy, ACS Nano 14 (2020) 13304–13315.
[41] G. Feng, H. Huang, M. Zhang, Z. Wu, D. Sun, Q. Chen, D. Yang, Y. Zheng, Y. Chen, X. Jing, Single atom iron-doped graphic-phase C_3N_4 semiconductor nanosheets for augmented sonodynamic melanoma therapy synergy with endowed chemodynamic effect, Adv. Sci. 10 (2023) e2302579.
[42] G. Yu, K. Gong, C. Xing, L. Hu, H. Huang, L. Gao, D. Wang, X. Li, Dual P-doped-site modified porous g-C_3N_4 achieves high dissociation and mobility efficiency for photocatalytic H_2O_2 production, Chem. Eng. J. 461 (2023) 142140.
[43] J. Feye, J. Matthias, A. Fischer, D. Rudolph, J. Treptow, R. Popescu, J. Franke, A. L. Exarhos, Z.A. Boekelheide, D. Gerthsen, C. Feldmann, P.W. Roesky, E.S. Rösch, SMART RHESINS-superparamagnetic magnetite architecture made of phenolic

resin hollow spheres coated with Eu(III) containing silica nanoparticles for future quantitative magnetic particle imaging applications, Small (2023) 2301997.
[44] X. Zhao, Q. Liu, X. Li, H. Li, Z. Shen, H. Ji, T. Ma, Exited state absorption upconversion induced by structural defects for photocatalysis with a breakthrough efficiency, Angew. Chem. Int. Ed. 62 (2023) e202219214.
[45] W. Wang, Q. Luo, L. Li, Y. Wang, X. Huo, S. Chen, X. Du, N. Wang, Ni-single-atom mediated 2d heterostructures for highly efficient uranyl photoreduction, Adv. Funct. Mater. 33 (2023) 2302913.
[46] M. Kwak, J. Bok, B.H. Lee, J. Kim, Y. Seo, S. Kim, H. Choi, W. Ko, W. Hooch Antink, C.W. Lee, G.H. Yim, H. Seung, C. Park, K.S. Lee, D.H. Kim, T. Hyeon, D. Yoo, Ni single atoms on carbon nitride for visible-light-promoted full heterogeneous dual catalysis, Chem. Sci. 13 (2022) 8536–8542.
[47] T. Liu, W. Zhu, N. Wang, K. Zhang, X. Wen, Y. Xing, Y. Li, Preparation of structure vacancy defect modified diatomic-layered g- C_3N_4 nanosheet with enhanced photocatalytic performance, Adv. Sci. 10 (2023) e2302503.
[48] R. Zou, Z. Chen, L. Zhong, W. Yang, T. Li, J. Gan, Y. Yang, Z. Chen, H. Lai, X. Li, C. Liu, S. Admassie, E.I. Iwuoha, J. Lu, X. Peng, Nanocellulose-assisted molecularly engineering of nitrogen deficient graphitic carbon nitride for selective biomass photo-oxidation, Adv. Funct. Mater. 33 (2023) 2301311.
[49] X. Di, Z. Pei, Y. Pei, T.D. James, Tumor microenvironment-oriented MOFs for chemodynamic therapy, Coord. Chem. Rev. 484 (2023) 215098.
[50] H. Liu, J. Wang, C. Song, K. Zhou, B. Yu, J. Jiang, J. Qian, X. Zhang, H. Wang, Exogenously triggered nanozyme for real-time magnetic resonance imaging-guided synergistic cascade tumor therapy, ACS Appl. Mater. Interfaces 14 (2022) 29650–29658.
[51] X. Zhu, J. Wu, R. Liu, H. Xiang, W. Zhang, Q. Chang, S. Wang, R. Jiang, F. Zhao, Q. Li, L. Huang, L. Yan, Y. Zhao, Engineering single-atom iron nanozymes with radiation-enhanced self-cascade catalysis and self-supplied H_2O_2 for radio-enzymatic therapy, ACS Nano 16 (2022) 18849–18862.
[52] H. Liu, C. Li, Y. Qian, L. Hu, J. Fang, W. Tong, R. Nie, Q. Chen, H. Wang, Magnetic-induced graphene quantum dots for imaging-guided photothermal therapy in the second near-infrared window, Biomaterials 232 (2020) 119700.